Acta Materialia 250 (2023) 118863

Contents lists available at ScienceDirect

Acta Materialia

journal homepage: www.elsevier.com/locate/actamat

Germanium monotelluride-based solid solutions as whole-visible dielectric-metallic-transition material platforms for programmable metasurfaces

Chaobin Bi [a,#], Lei Wang [b,#], Ruifan Li [a], Lin Zhao [a], Tianyu Xue [c], Chaoquan Hu [a,d,*], Xiaoyi Wang [d,*], Qidai Chen [b,*], Weitao Zheng [a,e,*]

[a] State Key Laboratory of Superhard Materials, Key Laboratory of Automobile Materials of Ministry of Education, School of Materials Science and Engineering, Jilin Provincial International Cooperation Key Laboratory of High-Efficiency Clean Energy Materials, Jilin University, Changchun 130012, China
[b] State Key Laboratory of Integrated Optoelectronics, College of Electronic Science and Engineering, Jilin University, Changchun 130012, China
[c] Center for High Pressure Science, State Key Lab of Metastable Materials Science and Technology, Yanshan University, Qinhuangdao 066004, China
[d] Key Laboratory of Optical System Advanced Manufacturing Technology, Changchun Institute of Optics, Fine Mechanics and Physics, Chinese Academy of Sciences, Changchun 130033, China
[e] State Key Laboratory of Automotive Simulation and Control, Jilin University, Changchun 130025, China

ARTICLE INFO

Keywords:
Germanium monotellurides
Solid solutions
Dielectric-metallic transition
Material platforms
Programmable metasurfaces

ABSTRACT

The development of next-generation programmable metasurfaces urgently requires phase change materials with dielectric-metallic transition (DMT-PCMs). Although DMT-PCMs in the infrared have been reported, DMT-PCMs in the visible spectrum are yet to be designed, limiting the nanophotonic applications of conventional programmable metasurfaces to the infrared band. Herein, we find that stoichiometric germanium monotelluride solid solutions, $Ge_{1-x}M_xTe$ (M = Sn, Sb, Pb, and Bi), have excellent DMT performance throughout the whole visible spectrum, and they can be used as versatile material platforms for fabricating programmable metasurfaces. As a proof-of-concept, the DMT performance of stoichiometric $Ge_{0.9}Sn_{0.1}Te$ solid solution is significantly superior to that of commonly studied non-stoichiometric PCMs (e.g., $Ge_2Sb_2Te_5$, Sb_2Te_3). Through a combination of experiments and first-principle calculations, we demonstrate that the high DMT performance of $Ge_{0.9}Sn_{0.1}Te$ derives from the unique bonding structure of the crystalline state with non-stoichiometric vacancy-free, high atomic number, and weak Sn-Te bonds, which is not present in conventional PCMs. Furthermore, using ultrashort-pulse lasers, we show that the crystalline $Ge_{0.9}Sn_{0.1}Te$ can be arbitrarily written, erased, and modified at the subwavelength level. The resonance peaks and colors of the $Ge_{0.9}Sn_{0.1}Te$-based grating metasurface can be continuously modulated over the whole visible spectrum. These results suggest that the DMT material platforms can be used to fabricate programmable metasurfaces. Therefore, this work presents a coherent report on the physical origin, material design, and photonic devices of DMT in the visible spectrum, which may extend the applications of programmable metasurfaces from the infrared band to the visible spectrum and inspire more researches.

1. Introduction

Phase change materials with dielectric-metallic transition (DMT-PCMs) have the characteristic that the real part of dielectric function (ε_1) rapidly decreases from positive to negative upon amorphous to crystalline phase transition (Fig. 1a) [1–6]. DMT-PCMs can undergo localized phase transitions induced by ultrashort-pulse lasers and form metasurfaces with alternating arrangements of dielectric amorphous and metallic crystalline states. Since the period/size/shape of nano-antennas can be arbitrarily and rapidly modified, such DMT-PCMs based metasurfaces are called "programmable" metasurfaces (PMS). Compared with conventional ion/electron beam etched metasurfaces, PMS holds great advantages of in-situ modulation of optical functions and dispensing with cumbersome multi-step nanofabrication [7–12].

* Corresponding authors.
E-mail addresses: cqhu@jlu.edu.cn (C. Hu), wangxiaoyi@163.com (X. Wang), chenqd@jlu.edu.cn (Q. Chen), wtzheng@jlu.edu.cn (W. Zheng).
# C.B. and L.W. contributed equally to this work.

https://doi.org/10.1016/j.actamat.2023.118863
Received 8 November 2022; Received in revised form 13 March 2023; Accepted 14 March 2023
Available online 20 March 2023

Although DMT-PCMs and PMS in the infrared band have been developed [1], DMT-PCMs and PMS covering the whole visible spectrum have not been designed, which greatly impedes the development of next-generation integrated optical switch [13–16], optical memory [17, 18], displayer [19,20], sensor [21], thermal emitter [22], filter [23], beam shaper [24,25], and other "programmable" nanophotonic devices [26–31].

Since most PCMs in amorphous phase exhibit a dielectric state [32–42], the key to designing DMT-PCMs is to make their crystalline phase exhibit a metallic state ($\varepsilon_1 < 0$) in the whole visible spectrum. However, this is not an easy task. The dielectric function (ε) of the material heavily relies on the interband and intraband transitions of electrons induced by the incident light (Eq. 1&2) [13,14,43-46]. According to the Tauc-Lorentz model (Eq. 3&4), the narrow optical bandgap E_g and the small broadening term C (i.e., high structural order) facilitates the redshift of interband transition absorption. Based on the Drude model (Eq. 5&6), the large carrier concentration n favors the blueshift of intraband transition absorption. Details of the Tauc-Lorentz and Drude models are in *Supplementary section* B2. Therefore, the ideal metallic crystalline phase should meet the three DMT requirements simultaneously: high structural order, narrow optical bandgap, and large carrier concentration. Although the effects of atomic composition of PCMs on the structural order, optical bandgap and carrier concentration have been sporadically reported in the literature, no effective methods have been proposed to satisfy the aforementioned DMT requirements.

$$\varepsilon_1(E) = \varepsilon_{1,\mathrm{TL}}(E) + \varepsilon_{1,\mathrm{D}}(E) \tag{1}$$

$$\varepsilon_2(E) = \varepsilon_{2,\mathrm{TL}}(E) + \varepsilon_{2,\mathrm{D}}(E) \tag{2}$$

$$\varepsilon_{1,\mathrm{TL}}(E)=\varepsilon_\infty+\frac{2}{\pi}\mathrm{P}\int_{Eg}^{\infty}\frac{\xi\cdot\varepsilon_{2,\mathrm{TL}}(\xi)}{\xi^2-E^2}d\xi \tag{3}$$

$$\varepsilon_{2,\mathrm{TL}}(E)=\begin{cases}\dfrac{AE_0C(E-Eg)^2}{\left(E^2-E_g\right)^2+C^2E^2}\dfrac{1}{E}\ \mathrm{for}E>Eg\\ 0\mathrm{for}E\le Eg\end{cases} \tag{4}$$

$$\varepsilon_{1,\mathrm{D}}(E)=1-\frac{\hbar^2 4\pi ne^2}{\left(E^2+\Gamma\mathrm{D}^2\right)\varepsilon_0 m^*} \tag{5}$$

$$\varepsilon_{2,\mathrm{D}}(E)=\frac{\hbar^2 4\pi ne^2\Gamma\mathrm{D}}{\left(E^3+\Gamma\mathrm{D}^2E\right)\varepsilon_0 m^*} \tag{6}$$

Of all chalcogenide phase change materials, the most widely studied is the DMT performance of pseudo-binary alloys, $(GeTe)_x$-$(Sb_2Te_3)_{1-x}$ [2, 4]. However, the DMT wavelength range of these materials fails to cover the whole visible spectrum. For example, $Ge_2Sb_2Te_5$ has DMT performance only in the limited visible range (400–615 nm), further limiting the optical modulation capability of its metasurfaces [2]. The DMT performance of Sb_2Te_3 is worse, with its DMT occurring only at 700–760 nm [4]. It is worth noting that both $Ge_2Sb_2Te_5$ and Sb_2Te_3 have non-stoichiometric vacancies, because of deviations from stoichiometry [47–49]. Non-stoichiometric vacancies inevitably reduce the structural order of $Ge_2Sb_2Te_5$ and Sb_2Te_3 [50,51], which in turn compromises the DMT performance (Eq. 3&4). Therefore, we envision that PCMs without non-stoichiometric vacancies, such as GeTe and its solid solutions, may be an effective way to obtain high DMT performance. However, current research into DMT performance has mainly focused on

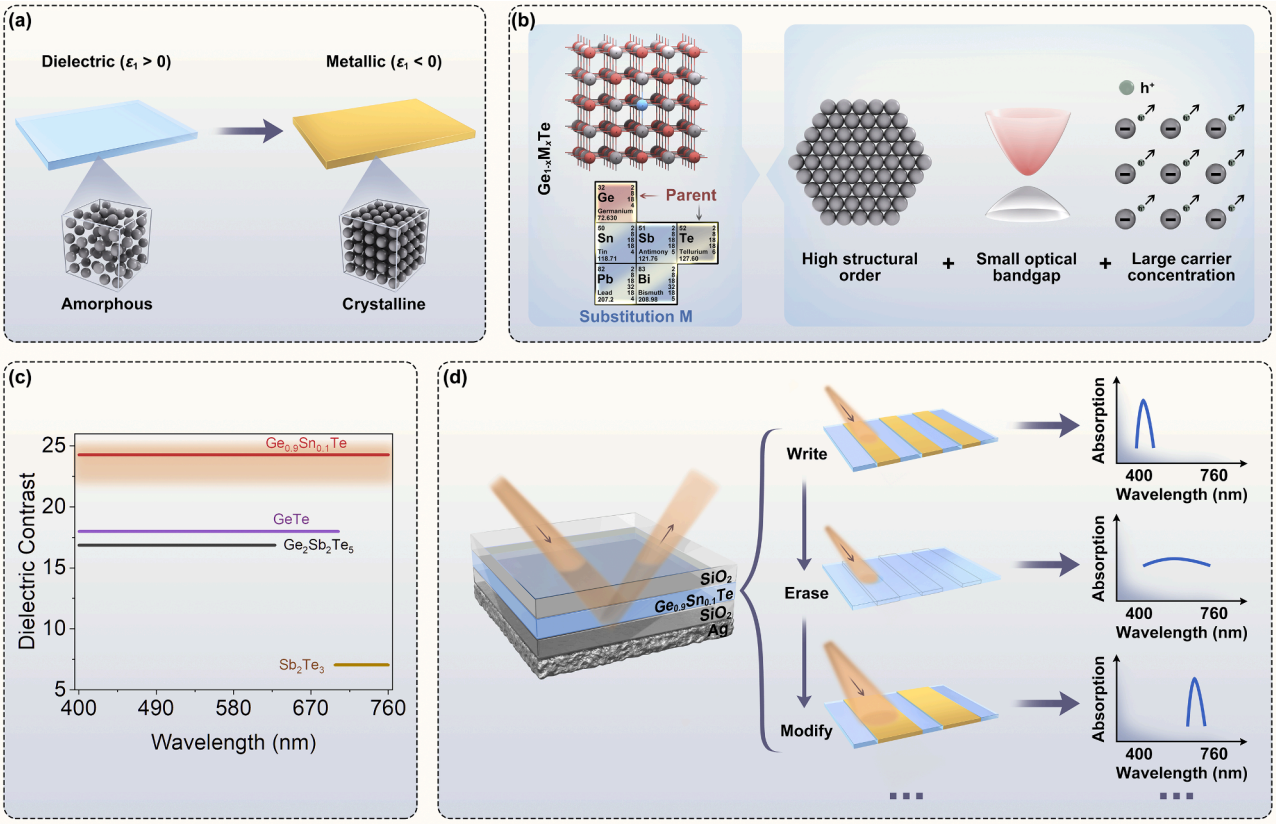

Fig. 1. Dielectric-metallic-transition (DMT) material platforms and their photonic applications. (a) The schematic diagram of phase change materials (PCMs) with dielectric amorphous phase and metallic crystalline phase. (b) The developed stoichiometric germanium monotelluride solid solutions with general formula of $Ge_{1-x}M_xTe$ (M = Sn, Sb, Pb and Bi). The heavy atom substitution for Ge in GeTe satisfy three DMT requirements: high structural order, narrow optical bandgap and large carrier concentration. (c) DMT wavelength range and dielectric contrast of $Ge_{0.9}Sn_{0.1}Te$ and literature reported materials. (d) The schematic diagram of the $Ge_{0.9}Sn_{0.1}Te$-based grating metasurface. The writing, erasing and modification of the grating, and the resulting change in absorption, are illustrated.

non-stoichiometric PCMs, with little attempt at stoichiometric PCMs.

In this work, we find germanium monotelluride-based solid solutions are versatile dielectric-metallic-transition material platforms, as their crystalline phase simultaneously fulfills three requirements: high structural order, narrow optical bandgap, and large carrier concentration (Fig. 1b). In contrast to previously reported DMT material platforms restricted to the infrared band, the material platforms we developed cover the whole visible spectrum. These DMT materials are not the commonly studied non-stoichiometric PCMs (e.g. $Ge_2Sb_2Te_5$, Sb_2Te_3), but solid solutions of standard stoichiometric PCMs (e.g. GeTe). In Sections 3.1 and 3.2, we reveal the microstructure of the $Ge_{0.9}Sn_{0.1}Te$ solid solution, and then demonstrate that its DMT performance is significantly better than that of the GeTe parent and non-stoichiometric $Ge_2Sb_2Te_5$ (Fig. 1c). In Sections 3.3 and 3.4, we analyze relationships among the bonding structure, intraband/interband transition absorption, and dielectric function, and reveal that the excellent DMT performance of $Ge_{0.9}Sn_{0.1}Te$ stems from the unique bonding structure of the crystalline phase with non-stoichiometric vacancy-free, high atomic number, and weak M-Te bonds, which are not found in conventional PCM. Based on new insights into the bonding structure, we propose design criteria for high-performance solid solutions and predict new candidate materials. In Sections 3.5 and 3.6, we demonstrate that crystalline $Ge_{0.9}Sn_{0.1}Te$ can be arbitrarily written, erased, and modified at the subwavelength scales with ultrashort-pulse lasers (Fig. 1d). The resonance peaks and colors of $Ge_{0.9}Sn_{0.1}Te$-based grating metasurfaces can be continuously modulated throughout the whole visible spectrum, an unachievable feature in conventional metasurfaces. Therefore, this work not only provides versatile DMT material platforms for programmable metasurfaces, but also establishes material design principles from the atomic level, which will the nanophotonic applications of programmable metasurfaces in the visible spectrum.

2. Materials and methods

2.1. Sample preparation

The $Ge_{1-x}Sn_xTe$ and $GeSe_xTe_{1-x}$ ($x = 0{\sim}1$) films were deposited on Si (001) and glass substrates by magnetron co-sputtering from GeTe target and SnTe, GeSe targets, respectively. GeTe and $Ge_2Sb_2Te_5$ films were deposited by sputtering of GeTe (80 W, RF) and $Ge_2Sb_2Te_5$ (80 W, RF) targets, respectively. The deposition was carried out in Ar atmosphere with the sputtering pressure and flow rate of 0.5 Pa and 50 sccm, respectively. The distance between substrates and the targets was 55 mm.

We prepared PCM film samples with a thickness of 200 nm by adjusting the deposition time. These thicker films are developed for two purposes: one for structural testing such as XRD and the other for reflectivity testing to obtain optical constants. A large thickness can ensure that the film is opaque to obtain high reflectivity. In addition, we also prepared the PCM layer with a thickness of 20 nm in our designed SiO_2/PCM/SiO_2/Ag device. The RF power applied to SnTe/GeSe targets was adjusted to 10, 20 and 30 W to prepared $Ge_{1-x}Sn_xTe/GeSe_xTe_{1-x}$ films with different x. For optical switching test and metasurface, SiO_2 layer was deposited by sputtering from SiO_2 (100 W, RF) target. For metasurface with structure of $SiO_2/Ge_{0.9}Sn_{0.1}Te/SiO_2$/Ag, Ag was deposited by sputtering from Ag (80 W, RF) target. After deposition, annealing was carried out in a pipe furnace in an Ar atmosphere to crystallize the films.

2.2. Structure and composition characterization

X-ray photoelectron spectroscopy (XPS, ESCALAB 250, Thermo-VG Scientific, America) and energy dispersive spectroscopy (EDS) equipped in the SEM (SU8010, HITACHI, Japan) were used for analyzing the chemical composition of samples. Bruker D8tools X-ray diffractometer (Cu Kα, $\theta-2\theta$ geometry) was used for grazing incidence X-ray diffraction (GIXRD) measurement. Atomic force microscope (Bruker, Inc., Dimension Icon) and Scanning Electron Microscope (SU8010, HITACHI, Japan) were used to characterize the surface morphology of the films. JEM-2100F (Field Emission) analytical electron microscope was used for taking picture of selected area electron diffraction (SAED) and high-resolution transmission electron microscopy (HRTEM) images.

2.3. Optical and electrical properties

The reflectance spectra in the range of 400 to 760 nm were measured by the UV–Vis-NIR spectrometer (Lambda 950, PerkinElmer, USA). The dielectric function was obtained by fitting reflectance spectra using Drude and Tauc-Lorentz dispersion models the electrical properties of the film such as carrier concentration and mobility were measured by Hall tester (CH Electronic devices, Inc., CH-50) (Supplementary Section B4). The absorption and reflectivity of metasurface were simulated using CST Microwave Studio (Supplementary Section D3).

2.4. First-principle calculations

First-principle calculations were performed within the framework of the density functional theory (DFT), as implemented in the Vienna *ab initio* simulation package (VASP). The Perdew-Burke-Ernzerhof (PBE) functional under the generalized gradient approximation (GGA) was chosen to describe the interactions between electrons. The energy cutoff of the plane wave is set to be 550 eV. The Brillouin zone was sampled in the gamma-centered grids with a k-point sampling density of 0.02 $\AA^{-1}$. All the structure we considered are relaxed under the convergence criteria of 10^{-4} eV (Supplementary Section C).

2.5. Ultrashort-pulse laser processing

The localized phase change of $Ge_{0.9}Sn_{0.1}Te$ was realized with a homebuilt ultra-short pulse laser processing system. A pulsed laser beam with wavelength of 514 nm and pulse width of 230 fs was provided by laser (Pharos, Light Conversion Ltd). When studying the switching properties of materials, we use a 20 × NA 0.4 objective lens with a spot diameter of about 1.570 um. To fabricate finer metasurface devices, we employ a 100 × NA 0.9 objective lens with a spot diameter of about 700 nm. The scanning speed of the laser can be calculated by $v = D \times \mathrm{Rep}/\mathrm{PN}$ where D is the spot diameter, Rep is the laser frequency (10 kHz), PN is the pulse number that is obtained from Fig. 4a. The above calculations reveal that the scanning speeds of the laser for erasing and writing are 200 and 0.8 um/s, respectively.

3. Results and discussion

3.1. The structure of $Ge_{0.9}Sn_{0.1}Te$

To obtain films with excellent dielectric-metallic transition (DMT) performance, we prepared and characterized $Ge_{1-x}Sn_xTe$ films with different Sn contents (x). Supplementary Fig. S16 shows real part of dielectric function (ε_1) of $Ge_{1-x}Sn_xTe$ films. With the increase of Sn content, ε_1 of the amorphous films decreases continuously, while ε_1 of the crystalline films decreases sharply at first and then remained almost unchanged. This indicates that $Ge_{0.9}Sn_{0.1}Te$ has the most variable ε_1 between amorphous and crystalline phases, and a lower ε_1 in crystalline phase. Therefore, we choose $Ge_{0.9}Sn_{0.1}Te$ to explore the DMT performance.

We further characterized the crystalline structure of $Ge_{0.9}Sn_{0.1}Te$. Fig. 2a shows the GIXRD spectra of c-$Ge_{0.9}Sn_{0.1}Te$ and rock-salt GeTe (c-GeTe) films. The (111), (200) (220) and (222) diffraction peaks of the rock-salt phase appear in both films, indicating c-$Ge_{0.9}Sn_{0.1}Te$ film has the same rock-salt structure as c-GeTe. Moreover, the diffraction peaks of the c-$Ge_{0.9}Sn_{0.1}Te$ film shift to lower angles compared with those of c-GeTe, which may be attributable to the increase of the lattice constant

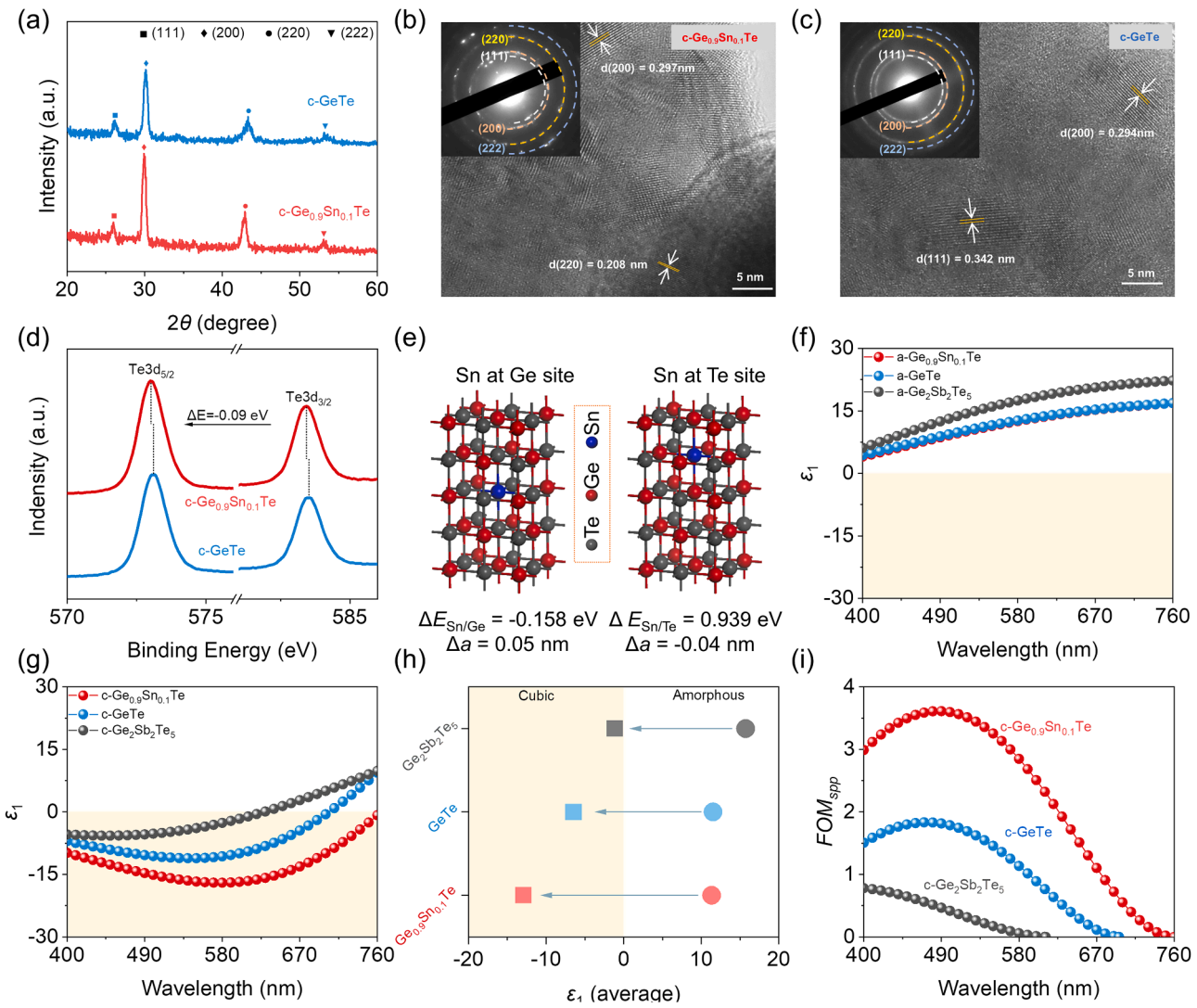

Fig. 2. Structure and the real part of dielectric function (ε1). (a) GIXRD spectra of c-Ge0.9Sn0.1Te and c-GeTe films. (b-c) SAED and HRTEM lattice images for (b) c-$Ge_{0.9}Sn_{0.1}Te$ and (c) c-GeTe films. (d) The XPS Te3d core-level spectra for c-$Ge_{0.9}Sn_{0.1}Te$ and c-GeTe films. (e) Schematic diagram for Sn in Ge site and Te site in GeTe unit cell. The Formation energy (ΔE) and the difference of lattice parameter (Δa) are given. (f-g) ε_1 in the whole visible spectrum (400–760 nm) for $Ge_{0.9}Sn_{0.1}Te$, GeTe and $Ge_2Sb_2Te_5$ films in (f) amorphous and (g) crystalline phases, respectively. (h) The average value of ε_1 in the whole visible spectrum for the three films. (i) FOM_{spp} for the three films in crystalline phase.

when the large-radius Sn atoms (145 pm) is substituted for the small-radius Ge atoms (125 pm). To further characterize the crystalline phase, SAED, HRTEM images and XPS spectra of the two films are presented in Fig. 2b-d. After incorporating Sn, the crystalline film still maintains the rock-salt structure, the (200) interplanar spacing increases from 0.294 nm to 0.297 nm, and the peak positions of $Te3d_{3/2}$ and $Te3_{d5/2}$ shift 0.09 eV to lower energy values. These results indicate that the substitution of low-electronegativity Sn (1.96) for Ge (2.01) leads to lattice expansion and formation of Sn-Te bonds. The formation energy and lattice constant, calculated from first principles for Sn at different positions in the GeTe, reveals that when Sn is substituted for Ge, the formation energy is smaller and the lattice constant is consistent with the experiment (Fig. 2e). These experiments together with first-principle calculations demonstrate that c-$Ge_{0.9}Sn_{0.1}Te$ is the GeTe-based solid solution with substitution of Sn for Ge.

3.2. High DMT performance in the whole visible spectrum

Fig. 2f-g shows the ε_1 of amorphous and crystalline $Ge_{0.9}Sn_{0.1}Te$ solid solution, GeTe parent and non-stoichiometric $Ge_2Sb_2Te_5$ films. ε_1 of the three amorphous films are positive in the whole visible spectrum (400–760 nm) and ε_1 of the three films change from positive to negative after crystallization, indicating that dielectric-metallic transition (DMT) occurs. DMT wavelength ranges of $Ge_{0.9}Sn_{0.1}Te$, GeTe and $Ge_2Sb_2Te_5$ films are 400–760 nm, 400–702 nm and 400–628 nm, respectively, and that of $Ge_2Sb_2Te_5$ is almost consistent with the literature report (400–615 nm) [2]. $Ge_{0.9}Sn_{0.1}Te$ films have much wider DMT wavelength range than GeTe and $Ge_2Sb_2Te_5$.

Fig. 2h shows the average ε_1 in the whole visible spectrum. The difference in average ε_1 of $Ge_{0.9}Sn_{0.1}Te$ in amorphous and crystalline phases is larger in comparison to that of GeTe and $Ge_2Sb_2Te_5$. The dielectric contrast of ε_1 ($\Delta\varepsilon_1$), namely the difference in average ε_1 between crystalline and amorphous phases, 24.3, 18.0 and 16.9 for $Ge_{0.9}Sn_{0.1}Te$, GeTe and $Ge_2Sb_2Te_5$ films, respectively. Figure of merit of surface plasmon-polaritons (FOM_{spp}) is defined as follow [52]:

$$FOM_{spp} = \frac{\mathrm{Re}(k_{spp})}{2\pi \cdot \mathrm{Im}(k_{spp})} \tag{7}$$

$$k_{spp} = k_0\sqrt{\frac{\varepsilon_{PCMs}\varepsilon_{vac}}{\varepsilon_{PCMs}+\varepsilon_{vac}}} \quad (8)$$

Where k_{spp} are the surface plasmon-polaritons (SPP) wavevector, $k_0 = 2\pi/\lambda_0$ is the free space wavevector, ε_{vac} is the dielectric constant of vacuum and its value is 1. FOM_{spp} characterizes the ability to support propagating SPP at an interface with vacuum. FOM_{spp} of $Ge_{0.9}Sn_{0.1}Te$ is 2.29, which is much higher than that of GeTe (1.18) and $Ge_2Sb_2Te_5$ (0.39) (Fig. 2i).

These results show that the DMT performance of $Ge_{0.9}Sn_{0.1}Te$ solid solution is higher than that of the GeTe parent and much higher than that of non-stoichiometric $Ge_2Sb_2Te_5$ reported previously. Therefore, $Ge_{0.9}Sn_{0.1}Te$ can be considered as a phase change material with excellent DMT performance in the whole visible spectrum, which we call the whole-visible DMT-PCMs.

3.3. Microscopic origin of high DMT performance

The ε_1 of the amorphous $Ge_{0.9}Sn_{0.1}Te$, GeTe, and $Ge_2Sb_2Te_5$ films at 400–760 nm are all greater than 0, indicating that they are in a dielectric state, which is in good agreement with the results in the literature. Therefore, the difference in the DMT performance of the three films is mainly attributed to the difference in ε_1 of the crystalline phase. In order to explain the excellent DMT performance of $Ge_{0.9}Sn_{0.1}Te$, we discussed the following two aspects: (1) Difference in ε_1 between crystalline GeTe parent and non-stoichiometric $Ge_2Sb_2Te_5$; (2) Difference in ε_1 between crystalline $Ge_{0.9}Sn_{0.1}Te$ solid solution and GeTe parent.

We first explored the reason why the ε_1 of c-GeTe is smaller than that of c-$Ge_2Sb_2Te_5$. By combining the Tauc-Lorentz with the Drude model, we fitted and analyzed the contribution of the model parameters to the difference in ε_1 between c-GeTe and c-$Ge_2Sb_2Te_5$ (Supplementary Section B2 and B3). Fig. 3a shows the curve of ε_1 corresponding to the model parameters and their contribution to the change of ε_1, with ε_1 of c-$Ge_2Sb_2Te_5$ taken as the initial reference. Only a decrease in broadening parameter C shifts the curve of ε_1 downwards and decreases the average value of ε_1. This indicates that the small ε_1 of c-GeTe, i.e. the high DMT performance of GeTe, is mainly attributed to the higher structural order of c-GeTe ($C = 1.21$ eV) than c-$Ge_2Sb_2Te_5$ ($C = 1.95$ eV). First-principle calculations were carried out to describe the differences in structural order. Both the bond lengths of Ge-Te and Sb-Te bonds in c-$Ge_2Sb_2Te_5$ follow Gaussian distribution (Fig. 3b), and the p-p orbital coupling strength is only 37% (Supplementary Section C3). In contrast, c-GeTe has uniform Ge-Te bond length and p-p orbital coupling strength of 39%, both of which confirm that c-GeTe has a higher structural order than c-$Ge_2Sb_2Te_5$. Numerous studies have shown that there are 20% non-stoichiometric vacancies randomly distributed in the cation sites in c-$Ge_2Sb_2Te_5$, which cause large Peierls distortion [48,53]. In contrast, c-GeTe has equal number of anions and cations and therefore higher structural order [54]. This contributes to the redshift of interband transition absorption and the reduction of ε_1 in the visible spectrum. Therefore, experiments and first-principle calculations are in good agreement, proving that the smaller ε_1 of c-GeTe compared with that of c-$Ge_2Sb_2Te_5$ is attributed to stoichiometric c-GeTe has higher structural order.

We then explored the reason why the ε_1 of c-$Ge_{0.9}Sn_{0.1}Te$ is smaller than that of c-GeTe. The structural order of c-$Ge_{0.9}Sn_{0.1}Te$ ($C = 1.19$ eV) is very close to that of c-GeTe ($C = 1.21$ eV), because c-$Ge_{0.9}Sn_{0.1}Te$ also has equal number of anions and cations. The optical bandgap ($E_g = 0.47$ eV) of $Ge_{0.9}Sn_{0.1}Te$ is narrower than that of GeTe ($E_g = 0.53$ eV), and the carrier concentration ($n = 28.7 \times 10^{20}$ cm^{-3}) is larger than that of GeTe ($n = 4.8 \times 10^{20}$ cm^{-3}). Fig. 3c shows the contribution of the Tauc-Lorentz and Drude model parameters to the ε_1 difference between c-$Ge_{0.9}Sn_{0.1}Te$ and c-GeTe. The smaller ε_1 of c-$Ge_{0.9}Sn_{0.1}Te$, that is, excellent DMT performance of $Ge_{0.9}Sn_{0.1}Te$, is attributable to the fact that the c-$Ge_{0.9}Sn_{0.1}Te$ has narrower optical bandgap and larger carrier concentration than c-GeTe while maintaining high structural order. The heavy atom substituted GeTe-based solid solutions satisfies "three DMT requirements".

We explored the origin of the narrow bandgap of $Ge_{0.9}Sn_{0.1}Te$ using DOS and XPS valence band spectra. The DOS of c-GeTe and c-$Ge_{0.9}Sn_{0.1}Te$ are mainly occupied by p orbitals, while s orbitals and d orbitals do not contribute at shallow energy levels (Supplementary Fig. S18). The substitution of Sn for Ge decreases bandgap from 0.388 eV to 0.158 eV, which is consistent with the fact that the fitted bandgap of

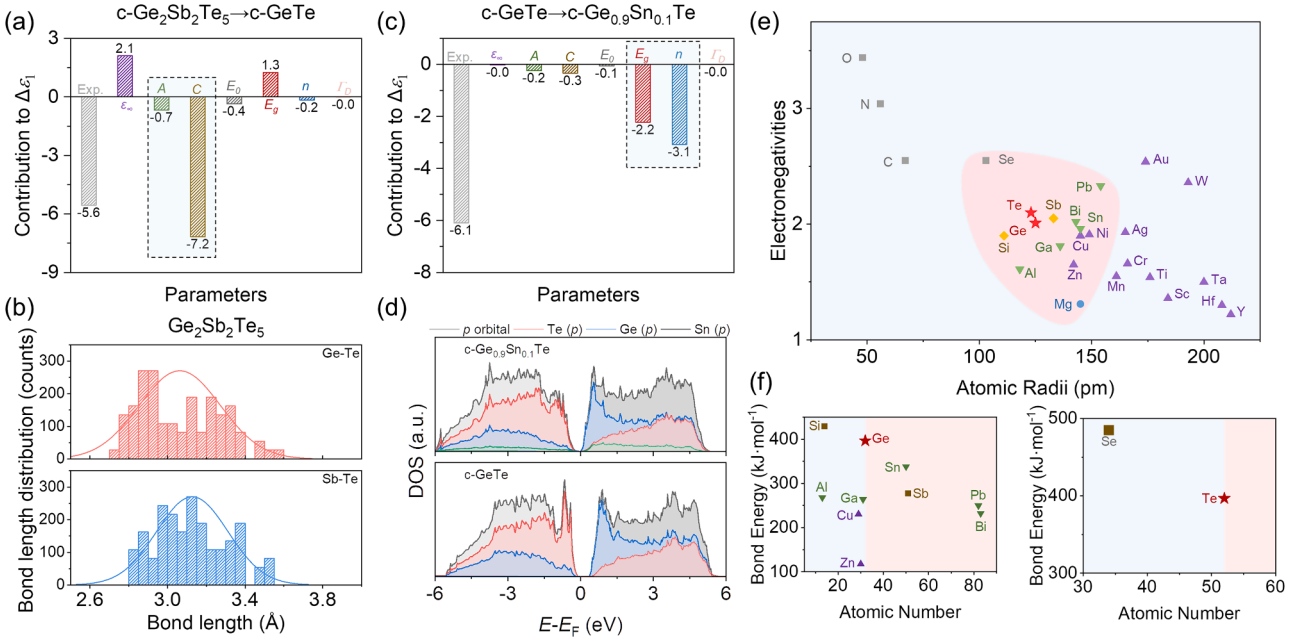

Fig. 3. Origin of excellent dielectric-metallic transition (DMT) performance and prediction of DMT materials. (a) Contributions of Tauc-Lorentz and Drude parameters to the ε1 between c-$Ge_2Sb_2Te_5$ and c-GeTe films. (b) Bond length distribution of Ge-Te and Sb-Te bonds in $Ge_2Sb_2Te_5$ supercell. (c) Contributions of Tauc-Lorentz and Drude parameters to the ε_1 between c-GeTe and c-$GeSe_{0.1}Te_{0.9}$ films. (d) PDOS for c-GeTe and c-$Ge_{0.9}Sb_{0.1}Te$ super cell. (e) Atomic radius and electronegativity of typical elements. (f) Atomic number and bond energy of selected elements.

$Ge_{0.9}Sn_{0.1}Te$ is narrower than that of GeTe. Further, PDOS shows that the substitution of Sn for Ge leads to the shift of the conduction band occupied by Ge-p orbitals towards the Fermi Level (Fig. 3d). Besides, the maximal binding energies of the valence band are found to be 0.23 eV and 0.15 eV for c-GeTe and c-$Ge_{0.9}Sn_{0.1}Te$ films, respectively, in the XPS valence band spectra. This indicates that the Fermi level position is pinned lower in the valance band edge as Sn is substituted for Ge, which decreases the band gap to some extent.

We also investigated the origin of the large carrier concentration in c-$Ge_{0.9}Sn_{0.1}Te$. Many studies have shown that although c-GeTe does not have non-stoichiometric vacancies caused by mismatch between anions and cations, it still has excess Ge vacancies caused by thermal vibration in room temperature [47,55]. This is because c-GeTe has an energetically unfavorable antibonding Ge-Te interactions in the highest occupied bands. Removal of Ge atoms is energetically favorable and generates holes, making c-GeTe a p-type semiconductor [51]. Therefore, the carrier concentration of c-GeTe is positively related to the Ge vacancy concentration, and the latter is highly dependent on the formation energy of Ge vacancies. We calculated the formation energy of one Ge vacancy in c-GeTe and c-$Ge_{0.9}Sn_{0.1}Te$ super cell. The results show that the formation energies of one Ge vacancy are 0.613 eV/unit and 0.228 eV/unit in c-GeTe and c-$Ge_{0.9}Sn_{0.1}Te$, respectively. Therefore, the substitution of Sn for Ge reduces formation energy of Ge vacancies, which increases the vacancy concentration of Ge, and in turn increases the carrier concentrations.

3.4. Design principles for DMT materials

Designing DMT materials is the key to enhancing the performance of both conventional and emerging nanophotonic applications, including all-optical switch [13–15], color rendering [19,20], sensing [21], and filter [23]. To meet the needs of DMT-PCMs in various applications, we propose design principles for DMT materials and suggest promising materials.

Through the above analysis of the reasons for the high DMT performance of $Ge_{0.9}Sn_{0.1}Te$, we reveal that designing heavy atom (M)-substituted GeTe-based solid solutions is an effective way to simultaneously satisfy the three DMT requirements: high structural order, narrow optical bandgap, and large carrier concentration. Experiments and first-principle calculations are in good agreement, confirming that the high structural order comes from the absence of non-stoichiometric vacancies, which reduces the Peierls distortion; the narrow optical bandgap comes from the substitution of Sn for Ge, which increases the average atomic number; the large carrier concentration arises from the substitution of low bond energy Sn-Te bond (359 kJ/mol) for the Ge-Te bond (397 kJ/mol), which reduces the vacancy formation energy and further increases vacancy concentration. Therefore, the design principles of proposed DMT-PCMs are as follows: non-stoichiometric vacancy-free, high average atomic number, and low bond energy.

We implement the above design principles with the heavy atom (M)-substituted GeTe-based solid solution ($Ge_{1-x}M_xTe$) and proposed candidate materials besides $Ge_{0.9}Sn_{0.1}Te$. First, we determine M by the formation conditions of the solid solution to meet the requirement of "non-stoichiometric vacancy-free". Fig. 3e shows the atomic radii and electronegativity values of typical elements. Mg, Al, Ga, Si, Sn, Zn, Cu, Ni, and Pb are more prone to be substituted for Ge to form solid solutions as their electronegativity values, atomic radii, and outer electron numbers are closer to those of Ge. Likewise, since electronegativity, atomic radius, and outer electron number of Se are closer to those of Te, Se tends to be substituted for Te to form solid solution. We then screened M with the criteria of "high average atomic number" and "low bond energy". Fig. 3f shows the average atomic number of $Ge_{1-x}M_xTe$ and the bond energy of M-Te. Sn, Sb, Pb and Bi were selected because of their higher atomic numbers and lower bond energy values. In contrast, Se is not a suitable candidate element because the atomic number of Se is smaller than that of Te and the bond energy of Ge-Se is higher than that of Ge-Te.

To verify the above hypothesis, we prepared $GeSe_xTe_{1-x}$ films with different doping concentrations in addition to $Ge_{1-x}Sn_xTe$. As shown in Supplementary Fig. S17, although $GeSe_{0.1}Te_{0.9}$ has the best DMT performance among $GeSe_xTe_{1-x}$ films, it is still worse than GeTe, which validates the hypothesis. Therefore, we propose that $Ge_{1-x}M_xTe$ (M = Sn, Sb, Pb and Bi) are excellent candidates of DMT-PCMs (Fig. 1b). $Ge_{1-x}Pb_xTe$ and $Ge_{1-x}Bi_xTe$ may have better DMT performance, which merits further study, as Pb and Bi are much heavier atoms than Ge and Sn, and the Pb-Te and Bi-Te bonds are much weaker.

3.5. Reversible optical switching

To evaluate the switching performance of the novel phase change material $Ge_{0.9}Sn_{0.1}Te$, we investigated the surface morphology and optical properties of the material induced by ultrashort-pulse lasers. Fig. 4a-c shows the change in microscopic surface morphology, SEM images, and optical images of amorphous films at different laser energies and frequencies. Four distinct areas can be observed. In region I, the morphology and optical properties of the films does not change, indicating that the film is still amorphous. In region II, the morphology changes and bright spots appear, indicating a transition from amorphous to crystalline phases. In regions III and IV, bumps and ablations appear. Therefore, the ultrashort-pulse laser was set as the condition in region II, that is 2500 pulses with 64.9 mJ/cm^2, to achieve crystallization (write). A similar approach was used to identify amorphizing conditions as shown in Supplementary Section D1. Laser was set to single pulse with 409 mJ/cm^2 to achieve amorphization (erase).

The lasers for crystallization (write) and amorphization (erase) are operated on as-deposited amorphous $Ge_{0.9}Sn_{0.1}Te$ film. Fig. 4d shows the optical image of dots that has been written and erased once to five times, where the bright area was crystalline and the dark area was amorphous. The recrystallized dots and as-deposited regions show a distinct interface, while the re-amorphous dots and as-deposited regions are well fused. Fig. 4e shows the optical image of "JLU" logo that has been written and erased five times. "JLU" logo is still very clear, indicating that the $Ge_{0.9}Sn_{0.1}Te$ film has good cycling stability. Details of the repeated writing and erasing can be seen in Movie S1. Fig. 4f shows the arbitrary writing and erasing of the grayscale images. "JLU" logo is written, erased, and converted to a "panda" pattern. "JLU" logo is almost invisible after erasing, while the newly written "panda" pattern is very clear. Details can be seen in Movie S2. In addition, by examining the change of transmittance with laser pulse width for $Ge_{0.9}Sn_{0.1}Te$ and GeTe films in the amorphous phase at different pulse energies, $Ge_{0.9}Sn_{0.1}Te$ shows a crystallization time not exceeding 300 ns and faster than that of GeTe (Supplementary Section D2). These results show that $Ge_{0.9}Sn_{0.1}Te$ has good cycling stability rewritable and modified features, and faster crystallization speed than GeTe, which is beneficial for practical applications. We find slight surface damage during PCM switching experiments. In this paper, we mainly reduce the surface damage caused by re-amorphization by introducing the SiO_2 layer. In the future, we will further reduce surface damage to achieve higher cycle life by optimizing the stacking quality of devices and reducing the degree of phase transition.

3.6. $Ge_{0.9}Sn_{0.1}Te$-based grating metasurface

To further explore the potential of DMT-PCMs in nanophotonic applications, we designed a $Ge_{0.9}Sn_{0.1}Te$-based grating metasurface, as shown in Fig. 5a. In the metasurface, $Ge_{0.9}Sn_{0.1}Te$ is sandwiched between 40-nm-thick SiO_2 layer and 120-nm-thick Ag layer. The dielectric amorphous and metallic crystalline $Ge_{0.9}Sn_{0.1}Te$ are alternately arranged by ultrashort-pulse lasers to form the grating. The SiO_2 layer acts as a spacer and the Ag layer acts as a mirror. Another 10-nm-thick SiO_2 layer is covered on the top to prevent oxidation of $Ge_{0.9}Sn_{0.1}Te$. Supplementary Fig. S22 shows the optical image of grating metasurface with

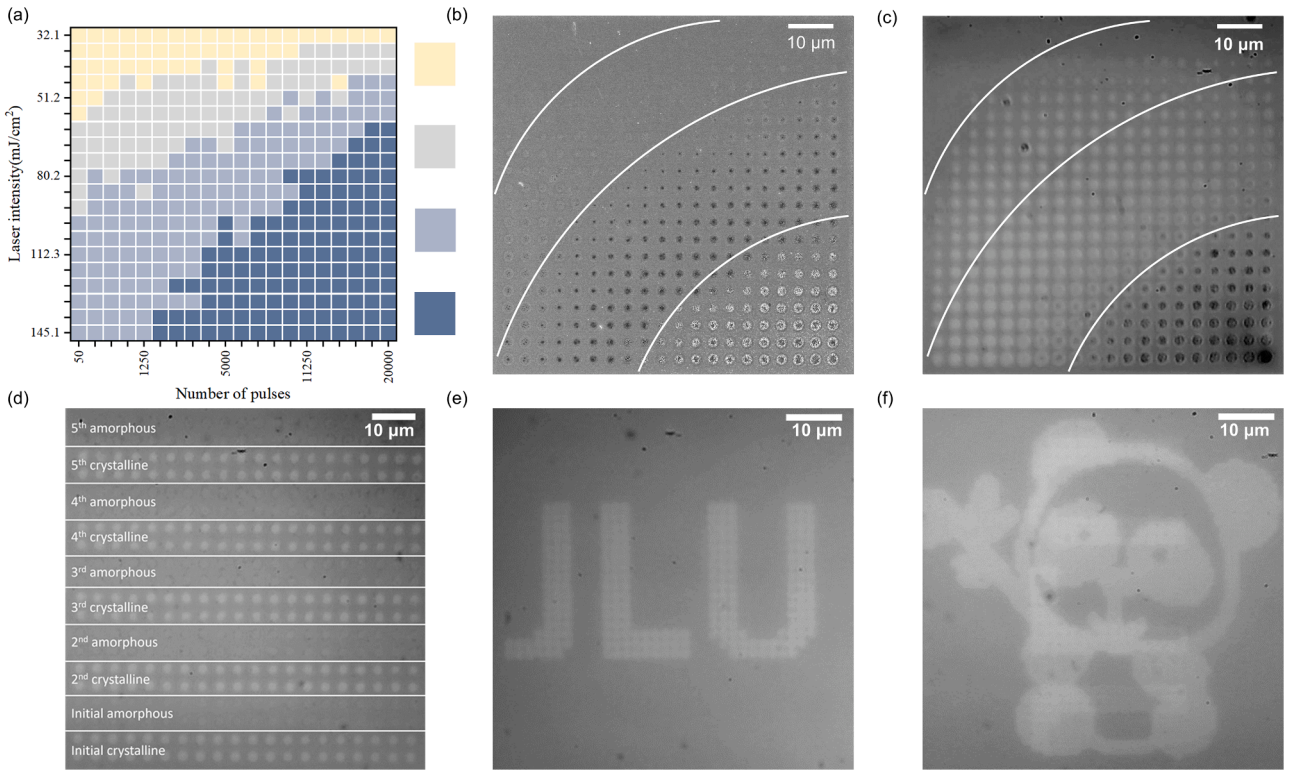

Fig. 4. Optical switching induced by ultrashort-pulse lasers. (a-c) (a) Change in surface morphology, (b) corresponding SEM and (c) optical images of different pulse parameter on as-deposited amorphous $Ge_{0.9}Sn_{0.1}Te$ film. (d-f) The optical image of as-deposited amorphous $Ge_{0.9}Sn_{0.1}Te$ film after laser crystallization (write) and amorphization (erase) operations. In (d), dots are written and erased from one to five times. In (e), "JLU" logo is written and erased five times. In (f), "JLU" logo is written and erased, and then the "panda" picture is written.

a typical grating period, with alternating arrangements of amorphous and crystalline $Ge_{0.9}Sn_{0.1}Te$, showing clear boundaries and periods. Supplementary Fig. S23 shows the experiment reflectance spectra of the typical sample and simulated reflectance spectra. The experimental reflectance spectra of amorphous, crystalline, and grating metasurface shows a consistent trend with the simulations, which means that the ultrashort-pulse lasers can produce the desired grating metasurface on DMT-PCMs. In this device, the possible optical losses mainly include the light absorption of the phase change material itself, the resonant absorption of the Fabry-Pérot cavity, and the local scattering caused by defects in the device.

We investigate the optical properties of $Ge_{0.9}Sn_{0.1}Te$-based grating metasurfaces with subwavelength periods. As seen in Fig. 5b, the resonance peak is located around wavelength of 400 nm when the period is 160 nm. As the period increases to 600 nm, the resonance peak gradually redshifts to wavelength of 760 nm, spanning the whole visible spectrum. The colors are plotted in CIE color gamut, as shown in Fig. 5d. Colors turns when periods change, and the color gamut is as high as 10% sRGB. For the $Ge_2Sb_2Te_5$-based grating metasurface with the same period, the resonance peak is much wider and shift from 404 nm to 710 nm, and the corresponding color gamut is only 5% sRGB (Fig. 5c-d).

Therefore, the $Ge_{0.9}Sn_{0.1}Te$-based metasurface has better optical modulation capability, thanks to the superior DMT performance of $Ge_{0.9}Sn_{0.1}Te$ over $Ge_2Sb_2Te_5$. In addition, compared with the "fixed" metasurface fabricated by ion/electron beam etching, the $Ge_{0.9}Sn_{0.1}Te$-based "programmable" metasurface is directly fabricated through partial phase transition from the dielectric amorphous to the metallic crystalline by laser pulses. The metasurface can be easily written, erased, and modified in situ, demonstrating unparalleled optical modulation performance.

Conclusions

We found stoichiometric germanium monotelluride solid solutions, $Ge_{1-x}M_xTe$ (M = Sn, Sb, Pb, and Bi), with excellent DMT performance over the whole visible spectrum, can serve as versatile material platforms for fabricating programmable metasurfaces. Through experiments and first-principle calculations of $Ge_{0.9}Sn_{0.1}Te$ solid solution, GeTe parent, and non-stoichiometric $Ge_2Sb_2Te_5$, we discuss the relationships among bonding structure, intraband/interband transition absorption, and dielectric function of PCMs. Based on new insights into bonding structures, we propose design principles for solid solutions with high DMT performance and predict new candidate materials. As an important step towards practical applications, we also explore the switching properties of $Ge_{1-x}M_xTe$ solid solution using ultrashort-pulse lasers and develop a grating metasurface based on the solution. The main conclusions are as follows:

(1) The crystalline $Ge_{0.9}Sn_{0.1}Te$ is a solid solution based on the rock-salt phase GeTe, in which Sn is substituted for Ge. Compared with GeTe parent and non-stoichiometric $Ge_2Sb_2Te_5$, $Ge_{0.9}Sn_{0.1}Te$ has the most excellent DMT performance, with DMT wavelength range, dielectric contrast and FOM_{SPP} as high as 400–760 nm, 24.3, and 2.29, respectively.

(2) The excellent DMT performance of $Ge_{0.9}Sn_{0.1}Te$ solid solution stems from the fact that the crystalline phase simultaneously satisfies three conditions: high structural order (C = 1.19 eV), narrow optical bandgap (E_g = 0.47 eV), and large carrier concentration ($n = 28.7 \times 10^{20}$ cm^{-3}). These three conditions originate from the lack of non-stoichiometric vacancies, high atomic number, and weak Sn-Te bonds, which are not present in either non-stoichiometric PCMs (such as $Ge_2Sb_2Te_5$) or standard stoichiometric GeTe. GeTe-based solid solutions with substitution of heavy atoms M (Sn, Sb, Pb and Bi) are all potential DMT-PCMs. In particular, $Ge_{1-x}Bi_xTe$ and $Ge_{1-x}Pb_xTe$ may exhibit

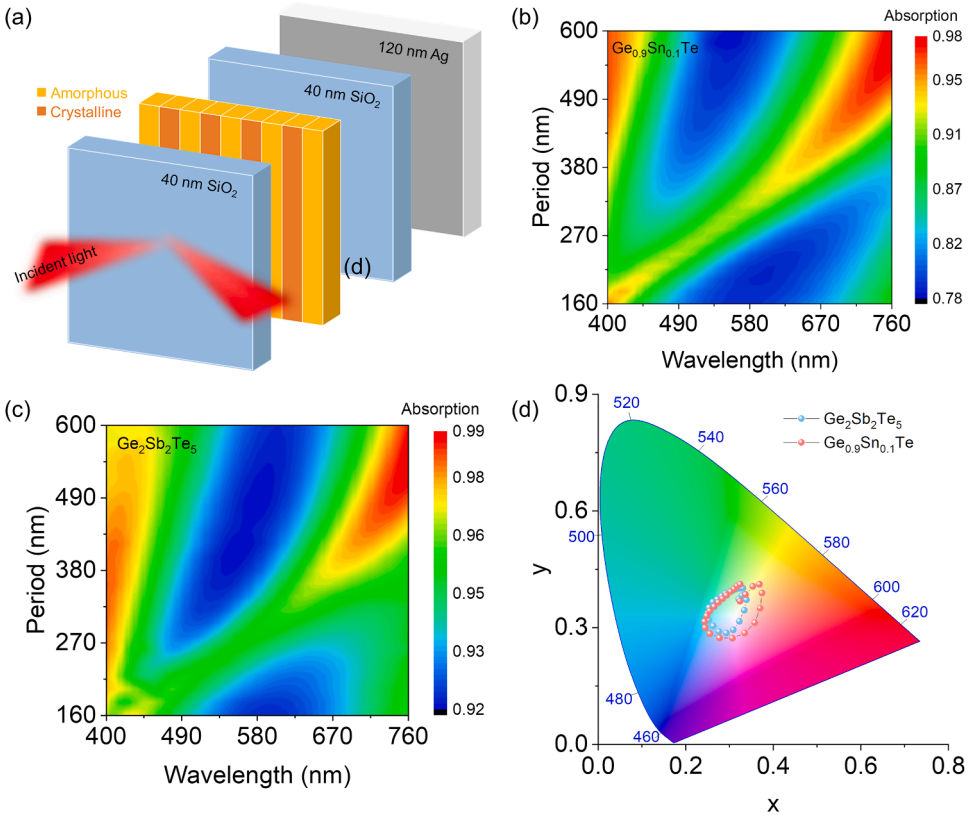

Fig. 5. The stacking and performance of grating metasurface. (a) The schematic diagram of the grating metasurface for color and absorption modulation. (b-d) The absorption for p-polarization light of (b) $Ge_{0.9}Sn_{0.1}Te$-based, (c) $Ge_2Sb_2Te_5$-based grating metasurface with grating period from 160 nm to 600 nm and (d) corresponding colors in CIE color gamut.

superior DMT than $Ge_{1-x}Sn_xTe$ and merit further verification.

(3) The crystalline $Ge_{0.9}Sn_{0.1}Te$ can be arbitrarily written, erased, and modified with ultrashort-pulse lasers, such as changing from "JLU" logo to "panda" pattern. $Ge_{0.9}Sn_{0.1}Te$ solid solution has good cycling stability and a faster crystallization speed than GeTe parent. In addition, the $Ge_{0.9}Sn_{0.1}Te$-based grating metasurface possesses optical modulation capability exceeding that of $Ge_2Sb_2Te_5$-based grating metasurface, and its resonance peak and color are continuously modulated in the entire visible light range.

(4) This work reports the physical origin, material design, and photonic devices of DMT in the visible spectrum. The developed DMT material platforms may extend the application of programmable metasurfaces from the infrared to the visible spectrum, which heralds new nanophotonic applications such as next-generation real-time biosensors, reprogramming detectors, and solar selective absorbers.

Declaration of Competing Interest

The authors declare no competing interests.

Acknowledgments

The authors gratefully acknowledge the financial support from National Natural Science Foundation of China (Grant Nos. 52272153, 52032004, 51932003) and KLOMT Key Laboratory Open Project (2022KLOMT02-05).

Supplementary materials

Supplementary material associated with this article can be found, in the online version, at doi:10.1016/j.actamat.2023.118863.

References

[1] A. Heßler, S. Wahl, T. Leuteritz, A. Antonopoulos, C. Stergianou, C.-F. Schön, L. Naumann, N. Eicker, M. Lewin, T.W.W. Maß, M. Wuttig, S. Linden, T. Taubner, In3SbTe2 as a programmable nanophotonics material platform for the infrared, Nat. Commun. 12 (2021) 924.
[2] B. Gholipour, A. Karvounis, J. Yin, C. Soci, K.F. MacDonald, N.I. Zheludev, Phase-change-driven dielectric-plasmonic transitions in chalcogenide metasurfaces, NPG Asia Mater. 10 (2018) 533–539.
[3] B.J. Kooi, M. Wuttig, Chalcogenides by design: functionality through metavalent bonding and confinement, Adv. Mater. 32 (2020), 1908302.
[4] K.V. Sreekanth, R. Medwal, C.M. Das, M. Gupta, M. Mishra, K.-T. Yong, R.S. Rawat, R. Singh, Electrically tunable all-PCM visible plasmonics, Nano Lett. 21 (2021) 4044–4050.
[5] Y. Xu, Y. Zhou, X.D. Wang, W. Zhang, E. Ma, V.L. Deringer, R. Mazzarello, Unraveling crystallization mechanisms and electronic structure of phase-change materials by large-scale ab initio simulations, Adv. Mater. 34 (2022), 2109139.
[6] P. Lazarenko, V. Kovalyuk, P. An, S. Kozyukhin, V. Takáts, A. Golikov, V. Glukhenkaya, Y. Vorobyov, T. Kulevoy, A. Prokhodtsov, A. Sherchenkov, G. Goltsman, Low power reconfigurable multilevel nanophotonic devices based on Sn-doped $Ge_2Sb_2Te_5$ thin films, Acta Mater. 234 (2022), 117994.
[7] S. Abdollahramezani, O. Hemmatyar, M. Taghinejad, H. Taghinejad, A. Krasnok, A. A. Eftekhar, C. Teichrib, S. Deshmukh, M.A. El-Sayed, E. Pop, M. Wuttig, A. Alù, W. Cai, A. Adibi, Electrically driven reprogrammable phase-change metasurface reaching 80% efficiency, Nat. Commun. 13 (2022) 1696.
[8] Z. Chen, M. Segev, Highlighting photonics: looking into the next decade, eLight (2021) 1.
[9] H.N.S. Krishnamoorthy, G. Adamo, J. Yin, V. Savinov, N.I. Zheludev, C. Soci, Infrared dielectric metamaterials from high refractive index chalcogenides, Nat. Commun. 11 (2020) 1692.
[10] Y. Wang, P. Landreman, D. Schoen, K. Okabe, A. Marshall, U. Celano, H.S.P. Wong, J. Park, M.L. Brongersma, Electrical tuning of phase-change antennas and metasurfaces, Nat. Nanotechnol. 16 (2021) 667–672.
[11] T. Cui, B. Bai, H.B. Sun, Tunable metasurfaces based on active materials, Adv. Funct. Mater. 29 (2019), 1806692.
[12] M.Y. Shalaginov, S. An, Y. Zhang, F. Yang, P. Su, V. Liberman, J.B. Chou, C. M. Roberts, M. Kang, C. Rios, Q. Du, C. Fowler, A. Agarwal, K.A. Richardson, C. Rivero-Baleine, H. Zhang, J. Hu, T. Gu, Reconfigurable all-dielectric metalens with diffraction-limited performance, Nat. Commun. 12 (2021) 1225.
[13] Y. Zhang, J.B. Chou, J. Li, H. Li, Q. Du, A. Yadav, S. Zhou, M.Y. Shalaginov, Z. Fang, H. Zhong, C. Roberts, P. Robinson, B. Bohlin, C. Ríos, H. Lin, M. Kang,

T. Gu, J. Warner, V. Liberman, K. Richardson, J. Hu, Broadband transparent optical phase change materials for high-performance nonvolatile photonics, Nat. Commun. 10 (2019) 4279.
[14] M. Delaney, I. Zeimpekis, D. Lawson, D.W. Hewak, O.L. Muskens, A new family of ultralow loss reversible phase-change materials for photonic integrated circuits: sb_2S_3 and Sb_2Se_3, Adv. Funct. Mater. 30 (2020), 2002447.
[15] Y. Zhang, C. Fowler, J. Liang, B. Azhar, M.Y. Shalaginov, S. Deckoff-Jones, S. An, J. B. Chou, C.M. Roberts, V. Liberman, M. Kang, C. Ríos, K.A. Richardson, C. Rivero-Baleine, T. Gu, H. Zhang, J. Hu, Electrically reconfigurable non-volatile metasurface using low-loss optical phase-change material, Nat. Nanotechnol. 16 (2021) 661–666.
[16] N. Youngblood, C. Ríos, E. Gemo, J. Feldmann, Z. Cheng, A. Baldycheva, W.H. P. Pernice, C.D. Wright, H. Bhaskaran, Tunable volatility of Ge2Sb2Te5 in integrated photonics, Adv. Funct. Mater. 29 (2019), 1807571.
[17] F. Yue, R. Piccoli, M.Y. Shalaginov, T. Gu, K.A. Richardson, R. Morandotti, J. Hu, L. Razzari, Nonlinear mid-infrared metasurface based on a phase-change material, Laser Photonics Rev 15 (2021), 2000373.
[18] Z. Cheng, C. Ríos, N. Youngblood, C.D. Wright, W.H.P. Pernice, H. Bhaskaran, Device-level photonic memories and logic applications using phase-change materials, Adv. Mater. 30 (2018), 1802435.
[19] P. Hosseini, C.D. Wright, H. Bhaskaran, An optoelectronic framework enabled by low-dimensional phase-change films, Nature 511 (2014) 206–211.
[20] H. Liu, W. Dong, H. Wang, L. Lu, Q. Ruan, Y.S. Tan, R.E. Simpson, J.K.W. Yang, Rewritable color nanoprints in antimony trisulfide films, Sci. Adv. 6 (2020) eabb7171.
[21] K.V. Sreekanth, S. Han, R. Singh, Ge2Sb2Te5-based tunable perfect absorber cavity with phase singularity at visible frequencies, Adv. Mater. 30 (2018), 1706696.
[22] Y. Kim, C. Kim, M. Lee, Parallel laser printing of a thermal emission pattern in a phase-change thin film cavity for infrared camouflage and security, Laser Photonics Rev. 16 (2021), 2100545.
[23] C. Ruiz de Galarreta, I. Sinev, A.M. Alexeev, P. Trofimov, K. Ladutenko, S. Garcia-Cuevas Carrillo, E. Gemo, A. Baldycheva, J. Bertolotti, C.David Wright, Reconfigurable multilevel control of hybrid all-dielectric phase-change metasurfaces, Optica 7 (2020) 2334–2536.
[24] X. Yin, T. Steinle, L. Huang, T. Taubner, M. Wuttig, T. Zentgraf, H. Giessen, Beam switching and bifocal zoom lensing using active plasmonic metasurfaces, Light Sci. Appl. 6 (2017) e17016-e17016.
[25] A. Leitis, A. Heßler, S. Wahl, M. Wuttig, T. Taubner, A. Tittl, H. Altug, All-dielectric programmable huygens' metasurfaces, Adv. Funct. Mater. 30 (2020), 1910259.
[26] M. Xu, X. Mai, J. Lin, W. Zhang, Y. Li, Y. He, H. Tong, X. Hou, P. Zhou, X. Miao, Recent advances on neuromorphic devices based on chalcogenide phase-change materials, Adv. Funct. Mater. 30 (2020), 2003419.
[27] D. Piccinotti, B. Gholipour, J. Yao, K.F. MacDonald, B.E. Hayden, N.I. Zheludev, Stoichiometric engineering of chalcogenide semiconductor alloys for nanophotonic applications, Adv. Mater. 31 (2019), 1807083.
[28] P. Pitchappa, A. Kumar, S. Prakash, H. Jani, T. Venkatesan, R. Singh, Chalcogenide phase change material for active terahertz photonics, Adv. Mater. 31 (2019), 1808157.
[29] M. Delaney, I. Zeimpekis, H. Du, X. Yan, M. Banakar, D.J. Thomson, D.W. Hewak, O.L. Muskens, Nonvolatile programmable silicon photonics using an ultralow-loss Sb_2Se_3 phase change material, Sci. Adv. 7 (2021) eabg3500.
[30] C. Hu, L. Ma, X. Li, Z. Liu, M. Cui, Y. Li, S. Li, X. Cao, Y. Zhang, J. Zhu, X. Wang, W. Zheng, Full-color, multi-level transmittance modulators: from reflectivity/gradient absorption coupling mechanism to materials map, Acta Mater. 216 (2021), 117132.
[31] C. Bi, K. Xu, C. Hu, L. Zhang, Z. Yang, S. Tao, W. Zheng, Three distinct optical-switching states in phase-change materials containing impurities: from physical origin to material design, J. Mater. Sci. Technol. 75 (2021) 118–125.
[32] M. Wuttig, V.L. Deringer, X. Gonze, C. Bichara, J.-Y. Raty, Incipient metals: functional materials with a unique bonding mechanism, Adv. Mater. 30 (2018), 1803777.
[33] W. Dong, H. Liu, J.K. Behera, L. Lu, R.J.H. Ng, K.V. Sreekanth, X. Zhou, J.K. W. Yang, R.E. Simpson, Wide bandgap phase change material tuned visible photonics, Adv. Funct. Mater. 29 (2018), 1806181.
[34] W. Zhang, R. Mazzarello, M. Wuttig, E. Ma, Designing crystallization in phase-change materials for universal memory and neuro-inspired computing, Nat. Rev. Mater. 4 (2019) 150–168.
[35] K. Konstantinou, T.H. Lee, F.C. Mocanu, S.R. Elliott, Origin of radiation tolerance in amorphous $Ge_2Sb_2Te_5$ phase-change random-access memory material, PNAS 115 (2018) 5353–5358.
[36] S. Cecchi, D. Dragoni, D. Kriegner, E. Tisbi, E. Zallo, F. Arciprete, V. Holý, M. Bernasconi, R. Calarco, Interplay between structural and thermoelectric properties in epitaxial $Sb_{2+x}Te_3$ alloys, Adv. Funct. Mater. 29 (2019), 1805184.
[37] Y.T. Liu, X.B. Li, H. Zheng, N.K. Chen, X.P. Wang, X.L. Zhang, H.B. Sun, S. Zhang, High-throughput screening for phase-change memory materials, Adv. Funct. Mater. 31 (2021), 2009803.
[38] M. Wuttig, C.F. Schön, M. Schumacher, J. Robertson, P. Golub, E. Bousquet, C. Gatti, J.Y. Raty, Halide perovskites: advanced photovoltaic materials empowered by a unique bonding mechanism, Adv. Funct. Mater. 32 (2021), 2110166.
[39] T.H. Lee, S.R. Elliott, Chemical bonding in chalcogenides: the concept of multicenter hyperbonding, Adv. Mater. 32 (2020), 2000340.
[40] B. Gholipour, The promise of phase-change materials, Science 366 (2019) 186–187.
[41] K. Konstantinou, F.C. Mocanu, J. Akola, S.R. Elliott, Electric-field-induced annihilation of localized gap defect states in amorphous phase-change memory materials, Acta Mater. 223 (2022).
[42] K. Konstantinou, S.R. Elliott, J. Akola, Inherent electron and hole trapping in amorphous phase-change memory materials: $Ge_2Sb_2Te_5$, J. Mater. Chem. C 10 (2022) 6744–6753.
[43] L. Guarneri, S. Jakobs, A. Hoegen, S. Maier, M. Xu, M. Zhu, S. Wahl, C. Teichrib, Y. Zhou, O. Cojocaru-Mirédin, M. Raghuwanshi, C.F. Schön, M. Drögeler, C. Stampfer, R.P.S.M. Lobo, A. Piarristeguy, A. Pradel, J.Y. Raty, M. Wuttig, Metavalent bonding in crystalline solids: how does it collapse? Adv. Mater. 33 (2021), 2102356.
[44] T. Siegrist, P. Jost, H. Volker, M. Woda, P. Merkelbach, C. Schlockermann, M. Wuttig, Disorder-induced localization in crystalline phase-change materials, Nat. Mater. 10 (2011) 202–208.
[45] C. Hu, J. Liu, J. Wang, Z. Gu, C. Li, Q. Li, Y. Li, S. Zhang, C. Bi, X. Fan, W. Zheng, New design for highly durable infrared-reflective coatings, Light Sci. Appl. 7 (2018) 17175.
[46] C. Hu, Z. Yang, C. Bi, H. Peng, L. Ma, C. Zhang, Z. Gu, J. Zhu, All-crystalline" phase transition in nonmetal doped germanium–antimony–tellurium films for high-temperature non-volatile photonic applications, Acta Mater. 188 (2020) 121–130.
[47] W. Zhang, A. Thiess, P. Zalden, R. Zeller, P.H. Dederichs, J.Y. Raty, M. Wuttig, S. Blugel, R. Mazzarello, Role of vacancies in metal-insulator transitions of crystalline phase-change materials, Nat. Mater. 11 (2012) 952–956.
[48] J.L.F. Da Silva, A. Walsh, H. Lee, Insights into the structure of the stable and metastable (GeTe)m(Sb2Te3)n compounds, Phys. Rev. B 78 (2008), 224111.
[49] Y. Zheng, M. Xia, Y. Cheng, F. Rao, K. Ding, W. Liu, Y. Jia, Z. Song, S. Feng, Direct observation of metastable face-centered cubic Sb_2Te_3 crystal, Nano Res. 9 (2016) 3453–3462.
[50] T.H. Lee, S.R. Elliott, Structural role of vacancies in the phase transition of $Ge_2Sb_2Te_5$ memory materials, Phys. Rev. B 84 (2011), 094124.
[51] M. Wuttig, D. Lusebrink, D. Wamwangi, W. Welnic, M. Gillessen, R. Dronskowski, The role of vacancies and local distortions in the design of new phase-change materials, Nat. Mater. 6 (2007) 122–128.
[52] G.V. Naik, V.M. Shalaev, A. Boltasseva, Alternative plasmonic materials: beyond gold and silver, Adv. Mater. 25 (2013) 3264–3294.
[53] S. Tao, Q. Li, J. Wang, X. Wang, J. Cai, S. Li, W. Xu, K. Zhang, C. Hu, Phase change materials for nonvolatile, solid-state reflective displays: from new structural design rules to enhanced color-changing performance, Adv. Opt. Mater. 8 (2020), 2000062.
[54] P. Martinez, V. Blanchet, D. Descamps, J.-B. Dory, C. Fourment, I. Papagiannouli, S. Petit, J.-Y. Raty, P. Noé, J. Gaudin, Sub-picosecond non-equilibrium states in the amorphous phase of GeTe phase-change material thin films, Adv. Mater. 33 (2021), 2102721.
[55] K. Singh, S. Kumari, H. Singh, N. Bala, P. Singh, A. Kumar, A. Thakur, A review on GeTe thin film-based phase-change materials, Appl. Nanosci. (2021) 1–16.